

Real-time Detection and Classification of Porous Bone Structures Using Image Segmentation and Opening Operation Techniques

Ching-Jung Hung, Yu-Reng Tsao, Chun-Li Lin, and Cheng-Yang Liu*

Department of Biomedical Engineering, National Yang Ming Chiao Tung University,
No. 155, Section 2, Linong Street, Beitou District, Taipei City 11221, Taiwan

(Received December 6, 2021; accepted March 29, 2022)

Keywords: porous bone material, image segmentation, opening operation

Porous bone structures with different lattices have great potential application in medical tissue engineering as they exhibit excellent mechanical properties. In this study, we utilize the optical microscope system as the optical sensor and imager to achieve real-time detection and categorization of pores bone materials based on machine learning techniques. The initial bone images are pictured using an industrial camera, and the image processes are compiled for defining the superficial shapes of the bone configuration. The image segmentation approaches contain Canny edge detection, k -means clustering, and binarization. The initial bone surface images are transformed into the gray-scale mode, and k -means clustering is utilized to normalize the gray-scale mode for enhancing binarization precision. The erosion and dilation of the opening operation are used to extract image noises and improve the pores characteristics. The profiles and the dimensions of the pores characteristics are precisely obtained by using Canny edge detection. The Gaussian blur method is performed to acquire obvious surface profiles of the pores configurations without background noise. The experimental results show that the geometric sizes of artificial pores implants can be clearly examined by this optical microscope system after metal additive manufacturing.

1. Introduction

In bone construction technology, therapeutic scaffolds with varied pores lattices are important to maintain the carrying of oxygen and nourishment and good organism and tissue ingrowths.^(1–3) Medical implants always undergo different mechanical stresses, including compression, tension, and torsion. Artificial implants with sufficient porosity should have a shape recoverable property.⁽⁴⁾ Therefore, bone characteristics, such as pores size, pores size distribution, pores morphology, pores orientation, and surface area-to-volume ratio, should be tailored for bone-tissue engineering applications.⁽⁵⁾ The mechanical qualities of artificial implants are improved by uniting micrometer-scale pores configurations into the scaffolds.⁽⁶⁾ The micrometer-scale pores structures also improve the cell adherence on the surface of the scaffold. Recently, three-dimensional printing (3DP) has been used to construct microscale metal pores

*Corresponding author: e-mail: cyliau66@nycu.edu.tw
<https://doi.org/10.18494/SAM3803>

structures by additive manufacturing.⁽⁷⁾ The micrometer-scale metal pores configurations with interconnected pores, intended dimension, and form can be immediately fabricated by employing 3DP. Hence, the categorization of pore dimension and form after 3DP is a major issue for configuration corrections and the accuracy of medical applications.

Digital image processing is a significant field in medical therapy and treatment.⁽⁸⁾ In clinical applications, the accurate segmentation of biomedical images is a fundamental step for monitoring, diagnosis, and therapy planning.⁽⁹⁾ In addition, accurate image segmentation is a critical method for pattern identification. The initial images are separated into various classifications on the basis of some standards that are utilized to obtain the location of interest. However, general segmentation by hand is a tedious operation and wastes time. A rapid automatic segmentation method with high resolution is needed for the treatment of a large number of therapeutic images. In 2009, the adaptive segmentation method with various thresholds was investigated for the definition and quantitative examination of natural and artificial pores structures.⁽¹⁰⁾ The direct image-derived porosities are clearly measured by the adaptive segmentation method. Furthermore, the geometrical parameters of metal cellular structures are evaluated by the segmentation and the skeletonization of the original images.⁽¹¹⁾ A suite of modules within the framework of the open-source image analysis program is used for the characterization of periodic pores structures.

In this work, the optical microscope system as the optical sensor and imager is used to achieve real-time detection and categorization of pores bone materials based on machine learning techniques. Multiple image segmentation methods are integrated with different advantages to categorize the raw pictures of the pores bone configurations. These image segmentation methods comprise Canny edge detection, binarization, and k -means clustering. The enhancement of image contrast based on erosion and dilation is implemented for the morphology of the pores bone structures.⁽¹²⁾ In these images, dilation attaches pixels to the pores borders, erosion withdraws pixels on the pores borders, and the noise in the pores images is eliminated by opening operation. Finally, the pores contours and diameters are pictured by utilizing the mathematical morphology of image segmentation methods.

2. Measurement Scheme and Methods

Figure 1(a) shows the experimental optical microscope system for capturing the initial surface pictures of the pores bone configurations. The optical microscope system includes a 12 mm objective lens (HM2012-10M) and a professional camera (Hayear HY-5200) with 4608×3456 pixels. The distance between the bone structure and the objective lens is about 90 mm. The pores surface of the bone structures is full of soft brightness by using a ring light (Hayear HY-209-144B). Uniform incidence of the ring light is advantageous for rugged surface imaging that completely excludes multiple reflections and metal surface shadows. The 24-bit captured images are saved in JPG format with 600×600 pixels. The dimension of the pixel in raw images is approximately $33.3 \mu\text{m}$. Three pores bone configurations are sketched through Materialise 3-matic with varied lattices and manufactured via direct laser metal sintering. In the 3DP manufacturing process, titanium alloy powder of Ti6Al4V is utilized with a $38 \mu\text{m}$ average grain

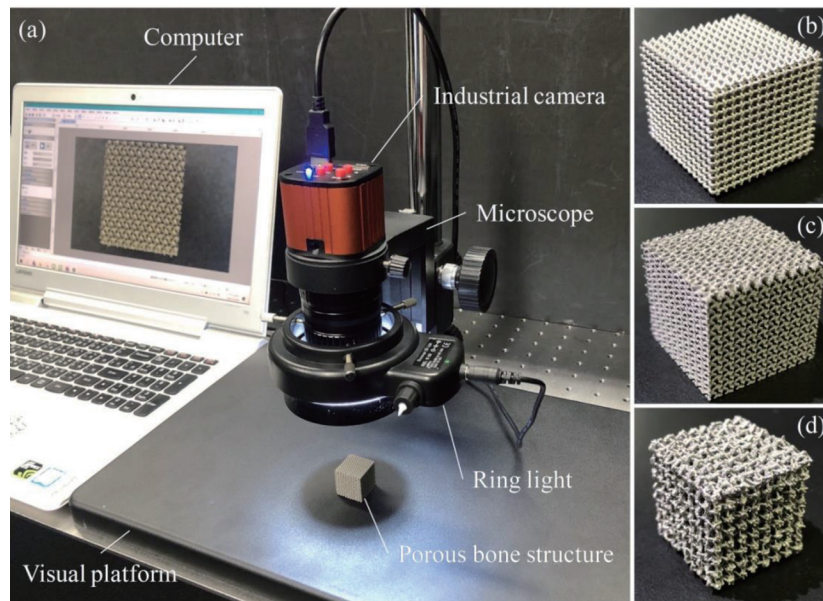


Fig. 1. (Color online) (a) Scientific optical microscope system for image acquisition. Selective porous metal bone configurations: (b) square array, (c) gyroid, and (d) random lattices.

diameter. Figures 1(b)–1(d) show the pictures of the pores metal bone configurations with three lattices. The pores sizes and diameters of the bone structures are in the range from 100 to 1600 μm . The nominal pores diameter is 500 μm . The pores metal bone configurations are manufactured without heating. The top surface of the bone structure is inspected by utilizing the optical microscope system. The computer program for image processing is based on Python 3.6. The computer equipment contains an Intel Core i7 central processing unit and 32 GB of random-access memory. The computation time of the image segmentation is 7.5 ms. The calculation program supplies a comfortable technique to implement the image segmentation and calculates a batch of raw pictures in a simple step.

Figure 2 shows the flowchart of the principal operations for the initial images. The purpose of the image operations is to determine the pores location and compute the pores diameter. The contours of the pores structure are separated from the background by image segmentation. The opening algorithms contain the morphological dilation and erosion. The Gaussian blur is used to eliminate the background noise. The final operation executes the statistical measurements for the whole surface of the pores configuration. The target of the image segmentation is to select the features of interest from the raw picture. Because the pores surface is abnormal and reflects light waves along chaotic directions, pores borders cannot constantly be distinguished. The cluster calculation is a graphic work of the principal analytic technique for mining data that identify the homogenous class of the object. This k -means calculation is a conventional data-clustering technique.^(13–15) The k -means clustering is exercised to categorize the gray gradient for gray-scale images. The processes of k -means clustering are as follows.

- (1) Resolve the k weights and collect information into k categories.
- (2) Choose k points randomly as a centroid from the dataset.
- (3) Compute the length between every centroid and point.

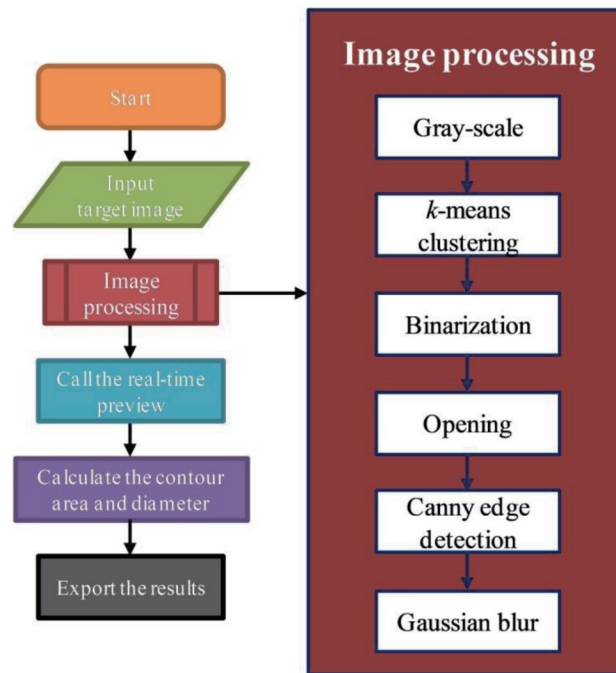


Fig. 2. (Color online) Flow diagrams of image processing.

- (4) Separate every point inside the category nearest a centroid.
- (5) Re-examine calculation to pick a new centroid while every centroid is clustered around a preset quantity of points.
- (6) Compare old and new centroids. If the length among old and new centroids is larger than a certain threshold, the location of the centroid is unstable. We need to iteratively execute the first to the third steps.
- (7) Conclude the calculation. If the length between old and new centroids is smaller than a certain threshold, the location of the remeasured centroid is stable.

The image binarization is subjected to black–white transformation from a gray-scale image after *k*-means clustering calculation.⁽¹⁶⁾ If the gray value is larger than a certain threshold, the pixels are changed to white in the image. Likewise, if the gray value is smaller than a certain threshold, the pixels are changed to black in the image. The binarization accuracy is promoted after the execution of *k*-means clustering.

The opening operation combines the dilation and erosion in the same structuring component, which mainly removes the slight noises in the image and isolates the borders of neighboring pores.⁽¹⁷⁾ The pores borders in the images are recognized by using Canny edge detection.^(18,19) This execution of Canny edge detection is shown as follows.

- (a) Resolve the gradient orientation and magnitude at every pixel in a raw picture.
- (b) If the gradient volume of one pixel is larger than those at two neighboring pixels in the gradient orientation, this pixel can be labeled as a border. Otherwise, this pixel is labeled as background.
- (c) Erase impotent borders through hysteresis thresholding.

The Gaussian blur is a low-pass filter for minimizing high-frequency noise.^(20,21) The noise degree is decreased, and effectiveness in the border detection is ameliorated.

3. Measurement Outcomes and Discussion

The presented method is utilized to measure three pores metal configurations. Figures 3 to 5 show the serial results of the image procedure for the pores bone configurations with three lattices. From Figs. 3(a), 4(a), and 5(a), it is observed that the initial raw images of these pores configurations have different strengths. The immediate thresholding of the initial images is required for binarization. The image segmentations are performed for the gray scaling. The intensities of the pixel in the gray scale correspond to the strut height. It can be seen in Figs. 3(b), 4(b), and 5(b) that the frameworks have neatly varying heights, but the pores configurations are expressed in random and high-frequency varieties. In Figs. 3(c), 4(c), and 5(c), the pixels belonged to pores, and frameworks are discriminated by *k*-means clustering calculations. A

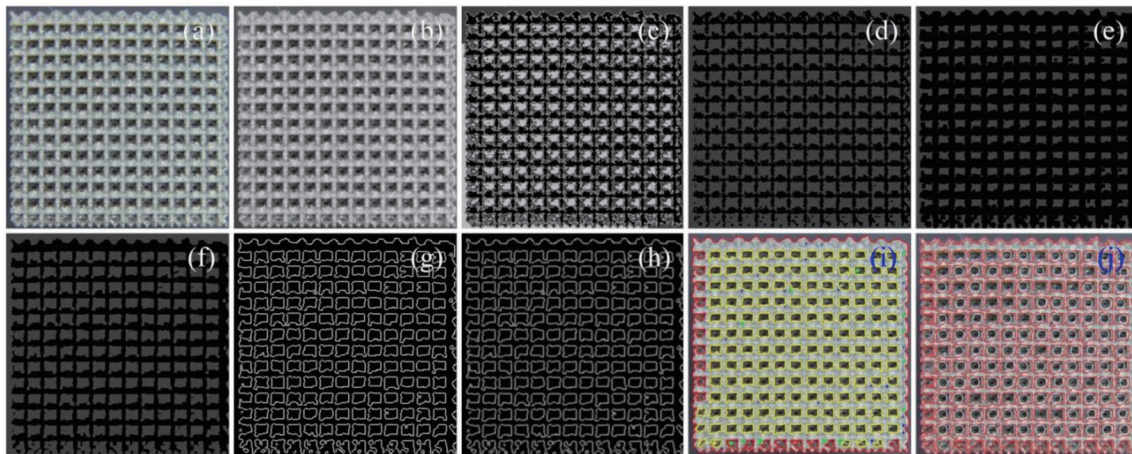


Fig. 3. (Color online) Experimental effects of the porous metal bone in square lattice: (a) initial image, (b) gray scaling, (c) *k*-means clustering, (d) binarization, (e) erosion, (f) dilation, (g) Canny edge detection, (h) Gaussian blur, (i) profile decision, and (j) dimension decision.

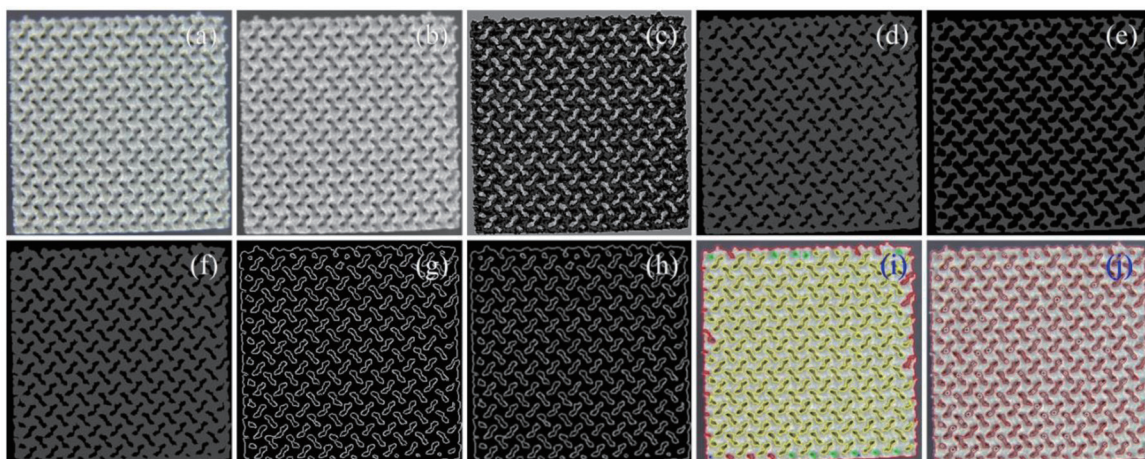


Fig. 4. (Color online) Experimental effects of the porous metal bone in gyroid lattice: (a) initial image, (b) gray scaling, (c) *k*-means clustering, (d) binarization, (e) erosion, (f) dilation, (g) Canny edge detection, (h) Gaussian blur, (i) profile decision, and (j) dimension decision.

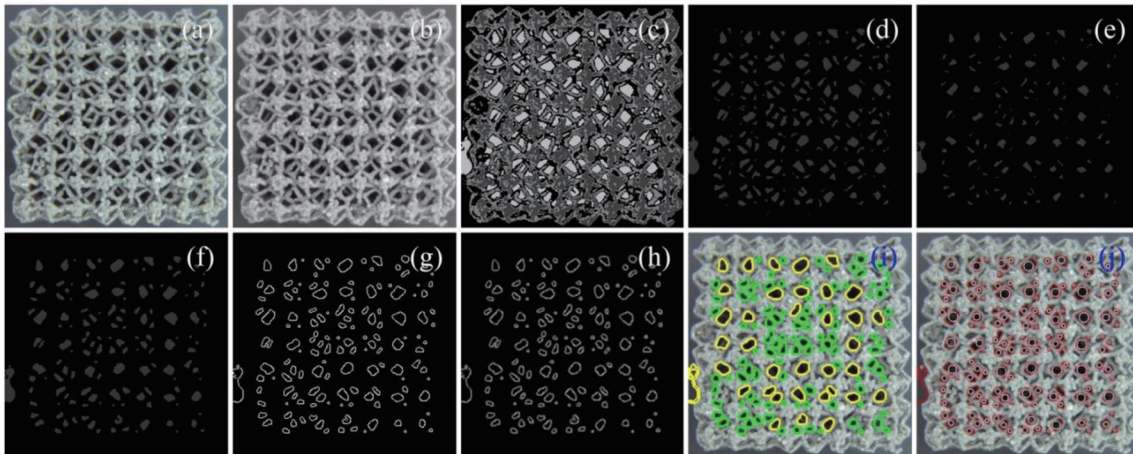


Fig. 5. (Color online) Experimental effects of the porous metal bone in random lattice: (a) initial image, (b) gray scaling, (c) *k*-means clustering, (d) binarization, (e) erosion, (f) dilation, (g) Canny edge detection, (h) Gaussian blur, (i) profile decision, and (j) dimension decision.

certain threshold could be simply applied to binarize the pixel values. Figures 3(d), 4(d), and 5(d) show the binarization of the images. It can be clearly seen that the pores locations are fairly bright when the background is dark. The results of the morphological erosion for the pores regions are shown in Figs. 3(e), 4(e), and 5(e). The results of the morphological dilation for the pores regions are shown in Figs. 3(f), 4(f), and 5(f). A succession of dilation and erosion eliminates the small-scale irregularities of the pores shapes. Figures 3(f), 4(f), and 5(f) show the gradient magnitudes of the pores regions. The images illustrate the gradients involving bright homogeneous borders in a black background.

A Canny edge detector with non-maximum oppression is used for obtaining pores edges, as shown in Figs. 3(g), 4(g), and 5(g). The pores edge contours are obtained by holding the minor borders that unite the major borders. As can be observed, the masses of the proper pores borders are identified from the binary images; however, a small quantity of the borders is lost owing to the division of the border boundaries. Figures 4(i) and 5(i) depict the discontinuities of the pores borders in the gyroid and random structures. Even if the image noises are insignificant and the pores borders are quite well described, the Canny edge detector loses a few features of the pores borders owing to the complicated profiles of random and gyroid configurations. Three pores configurations are tested for the execution of Canny edge detection. Although the quality of the pores borders has some deviations, the border contours are practically distinguished. Furthermore, the inscribed circles of the border contours are utilized to define the pores diameters. Figures 3(j), 4(j), and 5(j) depict the determinations of pores diameter. Every diameter of the pore is well clarified.

Figure 6 shows the classifications of the pores space and pores diameter of the square array configuration. As mentioned earlier, the circle diameter of the border contour is the length of the square lattice. It can be observed that 68% of the diameter values of the pores are in the range from 0.55 to 0.7 mm, and 80% of the area values of the pores are in the range from 0.6 to 0.75 mm². This aspect of the size distribution could be considered as a benchmark for the

following analysis of real structures. Figure 7 shows statistic histograms of pores space and diameter values in the gyroid configuration. The space distribution of the gyroid configuration shows two peaks nearly centered on 0.5 and 0.2 mm². By comparison, the diameter classification of the gyroid structure exhibits one peak around 0.35 mm. Figure 8(a) shows an exponential

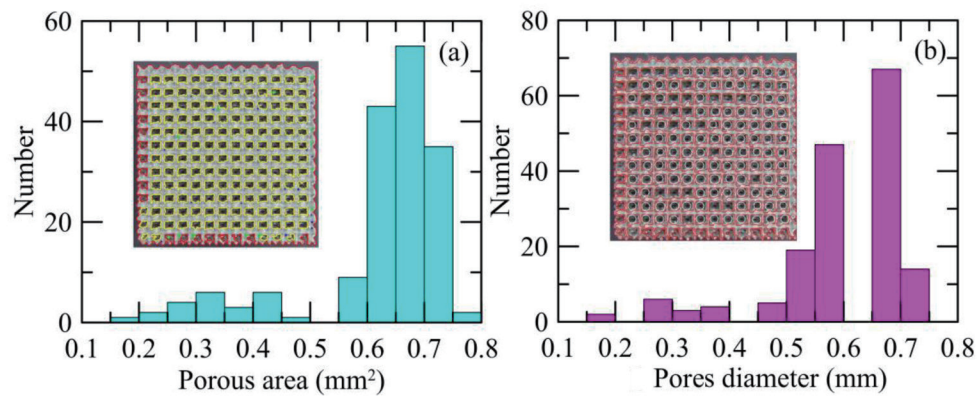


Fig. 6. (Color online) Classifications of (a) porous space and (b) pores diameter of the square array configuration.

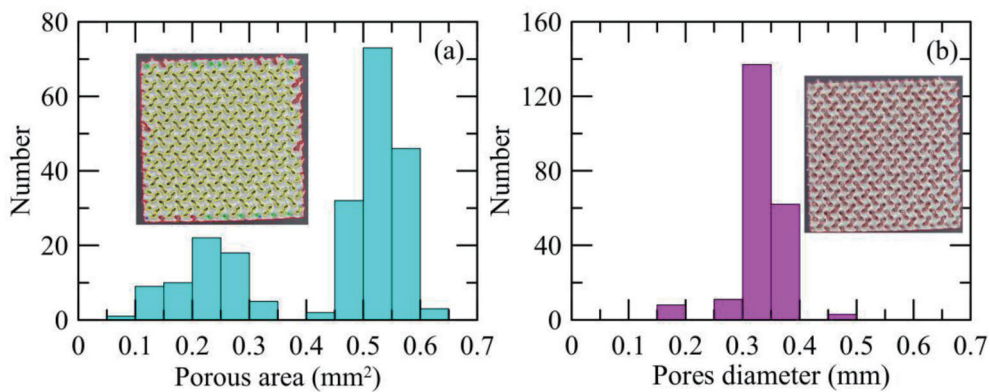


Fig. 7. (Color online) Classifications of (a) porous space and (b) pores diameter of the gyroid configuration.

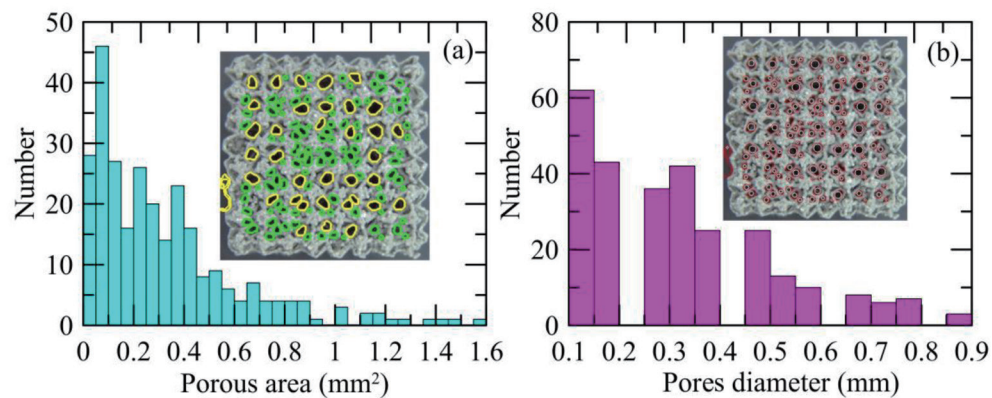


Fig. 8. (Color online) Classifications of (a) porous space and (b) pores diameter of the random configuration.

decay of the space distribution for the random pores configuration. The average zone of the random configuration is 0.324 mm^2 , and then the average diameter is 0.332 mm . Note that the lower peak of space classification for the random configuration agrees with the small pores diameters. The random borders are detected by high-accuracy image segmentation and opening operation methods. In previous studies, nondestructive imaging methods such as scanning electron microscopy (SEM) and X-ray computed tomography (CT) yielded high-resolution, three-dimensional measurements of periodic pores structures.^(10,11) However, adequate image segmentation methods for the conversion of gray-scale CT images should be developed for the quantitative characterization of pores features and subsequent modeling. In comparison with SEM and CT technologies, the presented system is less costly in terms of both price and computation speed.

4. Conclusions

In conclusion, an optical microscope system based on machine learning techniques is proposed for evaluating the geometrical properties of pores metal bone configurations produced by additive manufacturing. A suite of computation modules within the framework of the homemade code implements the inspection and classification of the pores types. To illustrate, the image segmentation is performed in the metal bone structures with three pores lattices. The pores borders are described visually, and the geometrical characteristics on a cluster of frameworks and pores are estimated at once. We achieved simultaneous image acquisition, classification, and exhibition of pores bone structures at a speed of 0.3 s . In comparison with general manual measurement methods, the geometries of porous areas and pores diameters are statistically quantified with a high degree of precision. The experimental results measured by our method may directly compare with the specifications of 3D patterns by computer-aided design. Moreover, this measurement arrangement can also be utilized for complex inspections of other medical productions.

Acknowledgments

This study was supported by Yen Tjing Ling Medical Foundation (CI-110-28) and the Ministry of Science and Technology of Taiwan (MOST 108-2221-E-010-012-MY3, MOST 109-2923-E-010-001-MY2).

References

- 1 S. Peltola, F. Melchels, D. Grijpma, and M. Kellomäki: *Ann. Med.* **40** (2008) 268. <https://doi.org/10.1080/07853890701881788>
- 2 A. Butscher, M. Böhner, S. Hofmann, L. Gauckler, and R. Müller: *Acta Biomater.* **7** (2011) 907. <https://doi.org/10.1016/j.actbio.2010.09.039>
- 3 H. Zhao, L. Li, S. Ding, C. Liu, and J. Ai: *Mater. Lett.* **223** (2018) 21. <https://doi.org/10.1016/j.matlet.2018.03.205>
- 4 S. Yunoki, E. Marukawa, T. Ikoma, S. Sotome, H. Fan, X. Zhang, K. Shinomiya, and J. Tanaka: *J. Mater. Sci.: Mater. Med.* **18** (2007) 2179. <https://doi.org/10.1007/s10856-007-3011-z>
- 5 A. Kumar, S. Mandal, S. Barui, R. Vasireddi, U. Gbureck, M. Gelinsky, and B. Basu: *Mater. Sci. Eng., R* **103** (2016) 1. <https://doi.org/10.1016/j.mser.2016.01.001>

- 6 H. Zhao and W. Liang: Mater. Lett. **194** (2017) 220. <https://doi.org/10.1016/j.matlet.2017.02.059>
- 7 J. Pucci, B. Christophe, J. Sisti, and E. Connolly Jr.: Biotechnol. Adv. **35** (2017) 521. <https://doi.org/10.1016/j.biotechadv.2017.05.007>
- 8 Y. Zhang: Advances in Image and Video Segmentation (Idea Group Publishing, USA, 2006).
- 9 H. Seo, M. Khuzani, V. Vasudevan, C. Huang, H. Ren, R. Xiao, X. Jia, and L. Xing: Med. Phys. **47** (2020) e148. <https://doi.org/10.1002/mp.13649>
- 10 P. Iassonov, T. Gebrenegus, and M. Tuller: Water Resour. Res. **45** (2009) W09415. <https://doi.org/10.1029/2009WR008087>
- 11 N. Vanderesse, I. Ky, F. González, N. Nuño, and P. Bocher: Mater. Des. **92** (2016) 767. <https://doi.org/10.1016/j.matdes.2015.12.062>
- 12 S. Thapar and S. Garg: Int. J. Comput. Bus. Res. **128** (2012) 2229. <https://api.semanticscholar.org/CorpusID:32294471>
- 13 T. Kanungo, D. Mount, N. Netanyahu, C. Piatko, R. Silverman, and A. Wu: IEEE Trans. Pattern Anal. Mach. Intell. **24** (2002) 881. <https://doi.org/10.1109/TPAMI.2002.1017616>
- 14 A. Likas, N. Vlassis, and J. Verbeek: Pattern Recognit. **36** (2003) 451. [https://doi.org/10.1016/S0031-3203\(02\)00060-2](https://doi.org/10.1016/S0031-3203(02)00060-2)
- 15 J. Yadav and M. Sharma: Int. J. Eng. Trends Technol. **4** (2013) 2972. <https://api.semanticscholar.org/CorpusID:61532973>
- 16 J. Sauvola and M. Pietikäinen: Pattern Recognit. **33** (2000) 225. [https://doi.org/10.1016/S0031-3203\(99\)00055-2](https://doi.org/10.1016/S0031-3203(99)00055-2)
- 17 R. Haralick, S. Sternberg, and X. Zhuang: IEEE Trans. Pattern Anal. Mach. Intell. **9** (1987) 532. <https://doi.org/10.1109/TPAMI.1987.4767941>
- 18 L. Ding and A. Goshtasby: Pattern Recognit. **34** (2001) 721. [https://doi.org/10.1016/S0031-3203\(00\)00023-6](https://doi.org/10.1016/S0031-3203(00)00023-6)
- 19 P. Bao, L. Zhang, and X. Wu: IEEE Trans. Pattern Anal. Mach. Intell. **27** (2005) 1485. <https://doi.org/10.1109/TPAMI.2005.173>
- 20 J. Flusser, S. Farokhi, C. Höschl, T. Suk, B. Zitová, and M. Pedone: IEEE Trans. Image Process. **25** (2015) 790. <https://doi.org/10.1109/TIP.2015.2512108>
- 21 J. Kostková, J. Flusser, M. Lébl, and M. Pedone: Pattern Recognit. **103** (2020) 107264. <https://doi.org/10.1016/j.patcog.2020.107264>

About the Authors



Ching-Jung Hung received his B.S. degree from National Ilan University, Taiwan in 2020. He is currently studying at National Yang Ming Chiao Tung University, Taiwan. His research interests are in opto-mechatronics systems and machine learning. (hleo6789@gmail.com)



Yu-Reng Tsao received his B.S. degree from Tamkang University, Taiwan in 2020. He is currently studying at National Yang Ming Chiao Tung University, Taiwan. His research interests are in opto-mechatronics systems and machine learning. (ivan93001@gmail.com)



Chun-Li Lin received his Ph.D. degree from National Cheng Kung University, Taiwan in 2000. From 2001 to 2010, he was a professor at Chang Gung University, Taiwan. Since 2010, he has been a professor at National Yang Ming Chiao Tung University, Taiwan. His research interests are in implant design and development, craniofacial biomechanics, and dental instruments and medical device development. (cclin2@nycu.edu.tw)



Cheng-Yang Liu received his Ph.D. degree from National Cheng Kung University, Taiwan in 2005. From 2010 to 2018, he was a professor at Tamkang University, Taiwan. Since 2018, he has been a professor at National Yang Ming Chiao Tung University, Taiwan. His research interests are in optomechanics systems, biomedical optics, biomechanics, and computer-aided design and manufacturing. (cylu66@nycu.edu.tw)